Supplementary information

Time-difference blow-spinning to a flexible dual-scale multilayer fabric for high-efficient electromagnetic interference shielding

Wei Song[1], Shuang Hu[1], Jiaxiang Lu[1,2], Liang Su[1], Zhemin Li[1], Junchen Liu[3,4], Yufeng Wu[4], Jianan Song[5], Zhenglian Liu[3], Shuaikai Xu[1*], Sen Lin[1,2*]

[1]School of Physical Science and Technology, Guangxi University, Nanning 530004, China.

[2]Advanced Institute for Brain and Intelligence, Guangxi University, Nanning 530004, China.

[3]State Key Laboratory of New Ceramics and Fine Processing, School of Materials Science and Engineering, Tsinghua University, Beijing 100084, China.

[4]State Key Laboratory of Information Photonics and Optical Communications and School of Science, Beijing University of Posts and Telecommunications, Beijing 100876, China.

[5]Sinochem Holdings Corporation Ltd., Xiongan 071000, China.

*Correspondence: slin@gxu.edu.cn (Sen Lin); skxu@gxu.edu.cn (Shuaikai Xu)

Supplementary Text

Statistics of MLPAN layer spacing

In order to measure the layer spacing of MLPAN, we collected 60-point data from cross-section SEM images at random positions, results are shown in Fig. S2. It is found that the layer spacing of MLPAN is mainly distributed in ~20 μm when the rotating speed was set as 2 degree per second.

XPS peak differentiation imitating analysis

XPS spectra peak differentiation imitating of Ti 2p and C 1s core levels of $Ti_3C_2T_x$ and $Ti_3C_2T_x$/MLPAN are shown in Fig. 2f and S7, details of binding energy are shown in Table S2. Ti 2p core level for both of them can be assigned into four doublets (Ti $2p_{3/2}$-Ti $2p_{1/2}$).[66] In the $Ti_3C_2T_x$, the C 1s core level can be fitted with six components centered at 291.4, 288.7, 286.2, 284.8, 282.3 and 281.8 eV, which can be assigned to π-π*, O-C=O, C-O, C-C, Ti-C-O and C-Ti bonds, respectively.[66,67] C 1s peak differentiation imitating for $Ti_3C_2T_x$/MLPAN distributed into seven components centered at 291.4, 288.7, 286.6, 286.2, 284.8, 282.3 and 281.8 eV, which can be assigned to π-π* hybridization, O-C=O, C≡N, C-O, C-C, Ti-C-O and C-Ti bonds, respectively.[66-68]

Electrical characteristics

IV/CV probe installation was used to measure the electrical characteristics of $Ti_3C_2T_x$/MLPAN. The conductivity and sheet resistance of materials can be calculated as follows:

$$\sigma = \frac{l}{RS} \quad \#(S1)$$

$$R_s = \frac{1}{\sigma t} \quad \#(S2)$$

where σ is conductivity, R is resistance of sample between two sides, S is cross sectional area, R_s is sheet resistance, t is thickness. The resistance, R, of sample can be calculated from corresponding volt-ampere characteristics with Ohm's law. The thickness, t, of sample can be measured by cross-section SEM. Particularly, R_s is different for different layers of $Ti_3C_2T_x$/MLPAN, which can be measured by exposing specific layer and appending strip electrodes on two opposite sides.

Electromagnetic interference (EMI) shielding characteristics

EMI shielding characteristics of as-prepared samples were measured via a 2-port vector network analyzer (PNA-L N5230C, Agilent Technologies, USA) with 8.2 to 12.4 GHz calibration kit. Before testing, all samples were cut into modular size (24 mm × 12 mm) and fixed in a square hollow waveguide (22.84 mm × 10.14 mm). Electromagnetic interference shielding effectiveness (EMI SE) in decibels (dB) can be defined as:[69,70]

$$SE\ (dB) = 10log\left(\frac{P_i}{P_t}\right) \#(S3)$$

where P_i and P_t are the power of incident wave and transmitted wave, respectively. The total SE (SE_{Total}) is defined as the sum of three terms include reflection loss (SE_R), absorption loss (SE_A), and multiple internal reflection loss (SE_M).[71] Particularly, SE_M for multilayer materials can be merged in the absorption loss due to the absorbed or dissipated of incident electromagnetic wave occurred in the shielding material.[31] Equation 6 and 7 in main text can also be derived from power coefficients relation as follows:

$$SE_R = 10log(\frac{1}{1-R}) \#(S4)$$

$$SE_A = 10log(\frac{1-R}{T}) \#(S5)$$

wherein, R is reflectivity and T is transmissivity. The corresponding power coefficients of R, T and absorptivity (A) follow the law of power balance:

$$R + T + A = 1 \#(S6)$$

The relations between power coefficients and S-parameters can be described as:

$$R = |S_{11}|^2 \ \#(S7)$$

$$T = |S_{21}|^2 \#(S8)$$

According to equation 10 in main text, defining Δ as the difference between the denominator and the numerator of the attenuation coefficient β, which is equal to:

$$\Delta = 1 + \left(e^{-\gamma t} - e^{-2\gamma t}\right)\Gamma_1^2 - e^{-\gamma t} \quad \#(S9)$$

wherein, considering that $\gamma t > 0$, $(e^{-\gamma t} - e^{-2\gamma t})$ is always greater than 0 and $e^{-\gamma t}$ is always less than 1. It can be seen that Δ is always greater than 0, and the attenuation coefficient β between 0 and 1, indicating the incident electromagnetic wave decays exponentially in conduction process.

CST electromagnetic simulations

Electromagnetic simulations were performed in computer simulation technology microwave studio (CST MWS 2019) based on a four-layer sandwich structure approximate model as shown in Fig. S21. The model consists two kinds of structures: the external high conductivity part (Z_I) and the internal low conductivity part (Z_{IV}), corresponding to different content of $Ti_3C_2T_x$ deposited on bilateral, and permeated inside. The material type of $Ti_3C_2T_x$ is

set to ohmic sheet, and the sheet resistances of the two parts for different $Ti_3C_2T_x$ content samples are respectively set to:

38.3 wt.%: Z_I = 2.25 Ω sq^{-1} and Z_{IV} = 1350.00 Ω sq^{-1};

49.6 wt.%: Z_I = 1.72 Ω sq^{-1} and Z_{IV} = 1025.00 Ω sq^{-1};

58.4 wt.%: Z_I = 0.58 Ω sq^{-1} and Z_{IV} = 712.00 Ω sq^{-1};

63.6 wt.%: Z_I = 0.38 Ω sq^{-1} and Z_{IV} = 520.00 Ω sq^{-1}

according to the test results. The electromagnetic characteristics of PAN layer (Z_{II}) and the gaps (Z_{III}) are both considered the same as air due to the aerogel-like structure of PAN. In this simulation, square hollow waveguide size conforms to its real size, and the electromagnetic waves travel in the negative direction of the *Z*-axis with the frequency of 8 to 12 GHz. All simulations were performed in time domain.

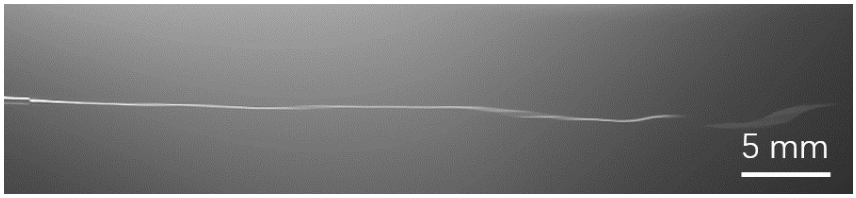

Fig. S1. High speed camera image of nozzle during time-difference blow-spinning.

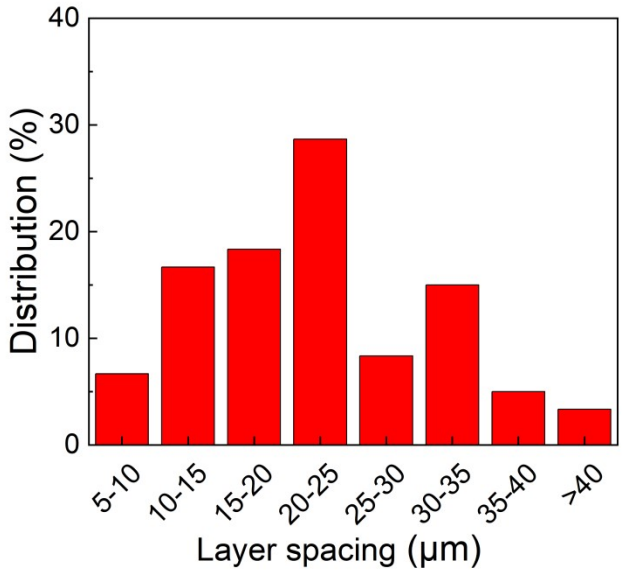

Fig. S2. Distribution of layer spacing of MLPAN measured by 60-point cross-section SEM images.

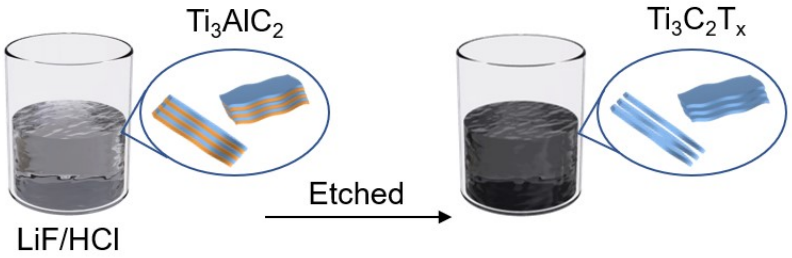

Fig. S3. The preparation process of $Ti_3C_2T_x$ by etching Ti_3AlC_2 in LiF/HCl.

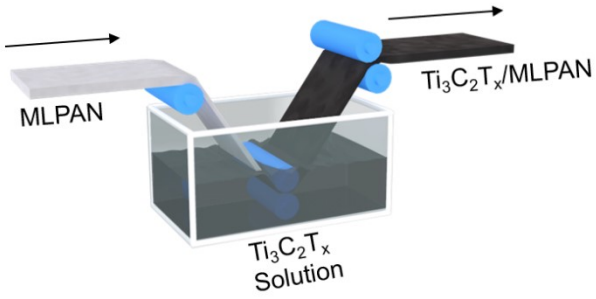

Fig. S4. A typical solution dip-coating process for conducting modification of MLPAN by $Ti_3C_2T_x$.

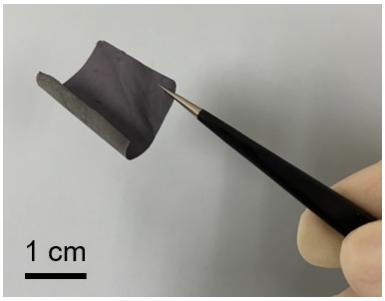

Fig. S5. Photographs of a flexible $Ti_3C_2T_x$/MLPAN hybrid fabric.

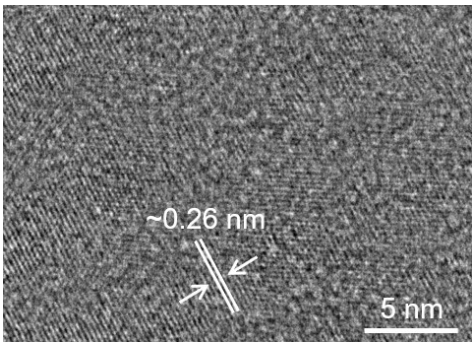

Fig. S6. HR-TEM image of a monolayer $Ti_3C_2T_x$ nanosheet.

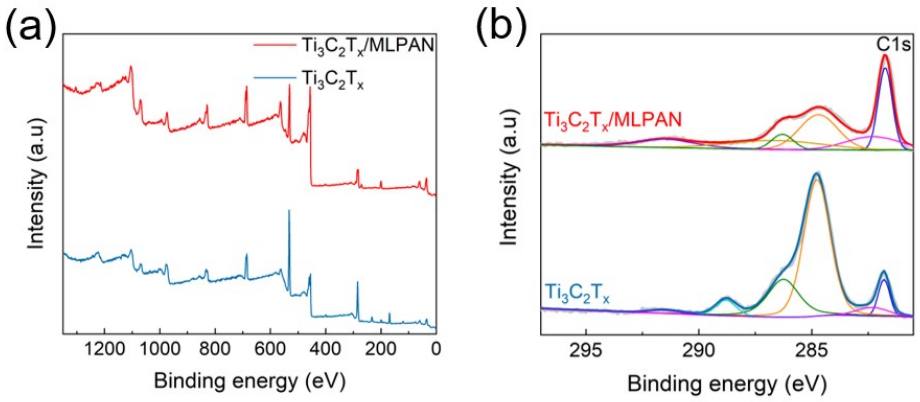

Fig. S7. XPS results of $Ti_3C_2T_x$ and $Ti_3C_2T_x$/MLPAN include (a) survey, and (b) peak differentiation imitating analysis of C1s.

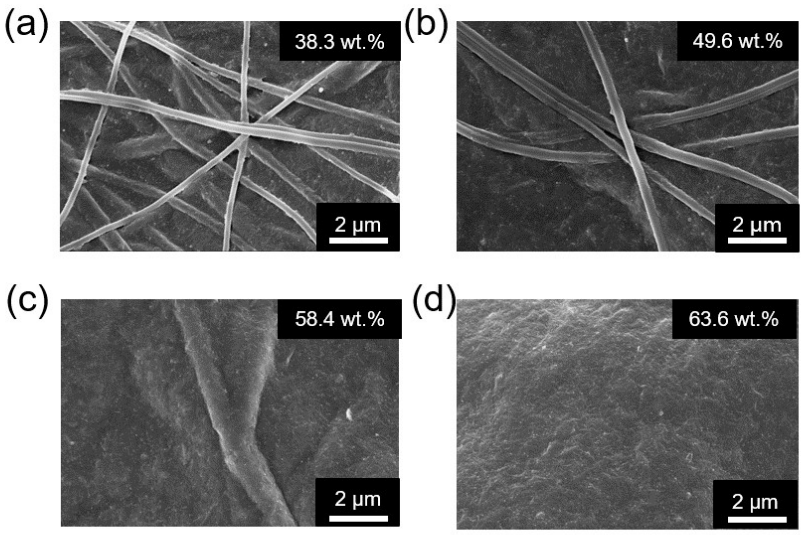

Fig. S8. Zoom-in surface SEM images of $Ti_3C_2T_x$/MLPAN with different $Ti_3C_2T_x$ content of (a) 38。2 wt.%, (b) 49.6 wt.%, (c) 58.4 wt.% and (d) 63.6 wt.%.

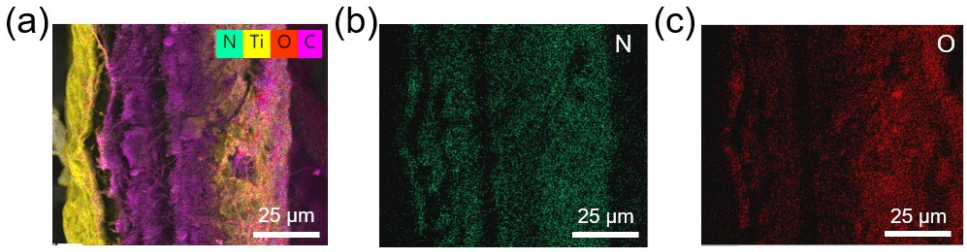

Fig. S9. Cross-section EDS elemental mapping results of $Ti_3C_2T_x$/MLPAN include (a) survey, (b) N, and (c) O.

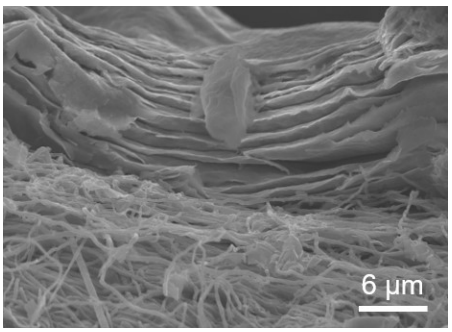

Fig. S10. Cross-section SEM image of $Ti_3C_2T_x$/MLPAN around compound interface.

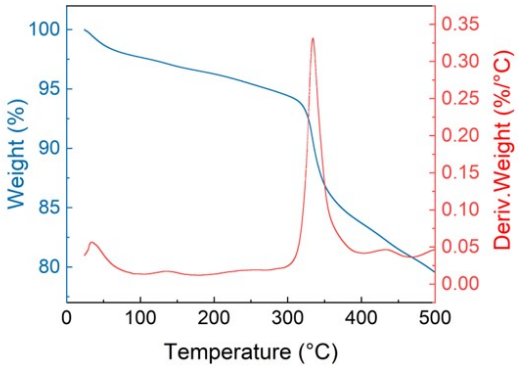

Fig. S11. TGA (blue) and DTG (red) of $Ti_3C_2T_x$/MLPAN.

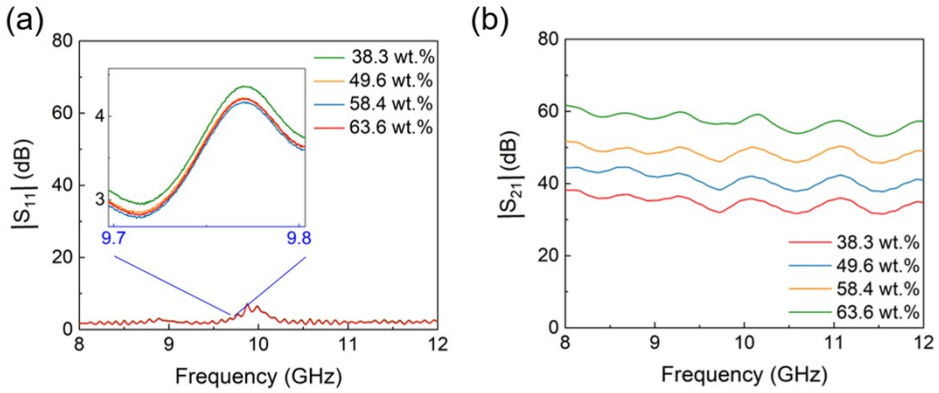

Fig. S12. S-parameters include (a) $|S_{11}|$ and (b) $|S_{21}|$ of $Ti_3C_2T_x$/MLPAN with different $Ti_3C_2T_x$ content of 38.3 wt.%, 49.6 wt.%, 58.4 wt.% and 63.6 wt.%.

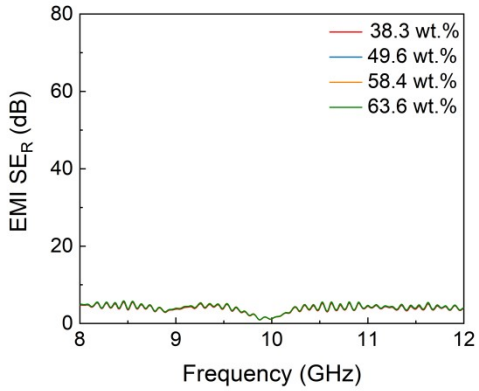

Fig. S13. SE_R of $Ti_3C_2T_x$/MLPAN with different $Ti_3C_2T_x$ content of 38.3 wt.%, 49.6 wt.%, 58.4 wt.% and 63.6 wt.%.

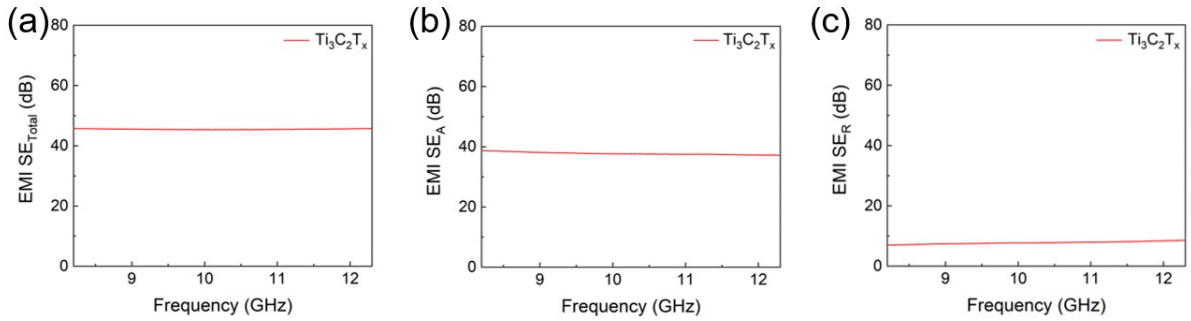

Fig. S14. EMI SE of $Ti_3C_2T_x$ extraction film, (a) EMI SE_{Total}, (b) EMI SE_A, (c) EMI SE_R. The $Ti_3C_2T_x$ thin-film mass was approximately 4.4 mg. In the $Ti_3C_2T_x$/MLPAN with a $Ti_3C_2T_x$ content of 63.6 wt.%, the $Ti_3C_2T_x$ mass used was approximately 4.3 mg.

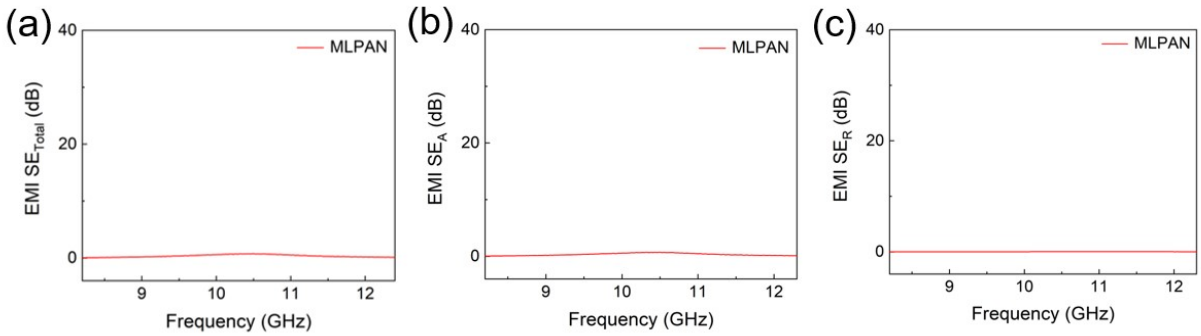

Fig. S15. EMI SE of MLPAN include (a) EMI SE_{Total}, (b) EMI SE_A, and (c) EMI SE_R.

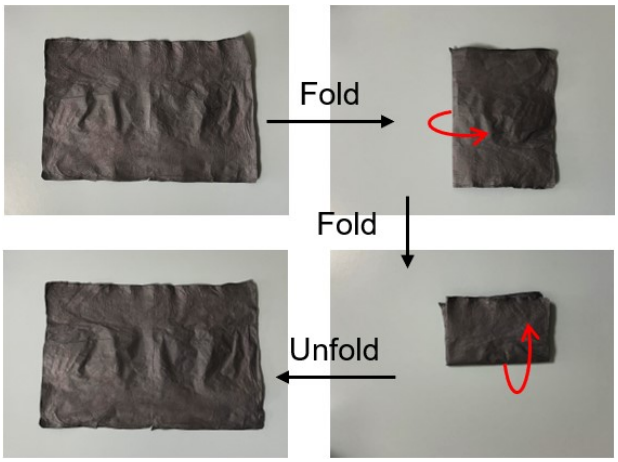

Fig. S16. Folding demonstration of as-prepared $Ti_3C_2T_x$/MLPAN hybrid fabric.

Fig. S17. Coiling demonstration of as-prepared $Ti_3C_2T_x$/MLPAN hybrid fabric.

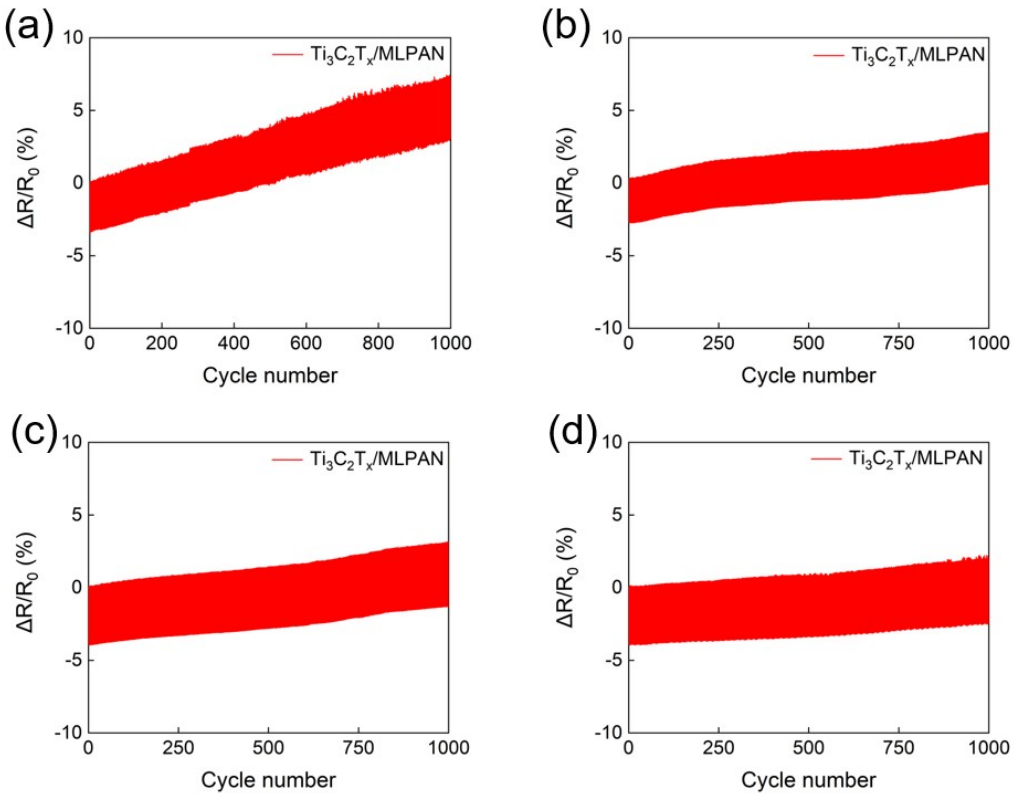

Fig. S18. Real-time resistance changes of $Ti_3C_2T_x$/MLPAN with different $Ti_3C_2T_x$ content of (a) 38.3 wt.%, (b) 49.6 wt.%, (c) 58.4 wt.% and (d) 63.6 wt.% during 1000-cycle bending.

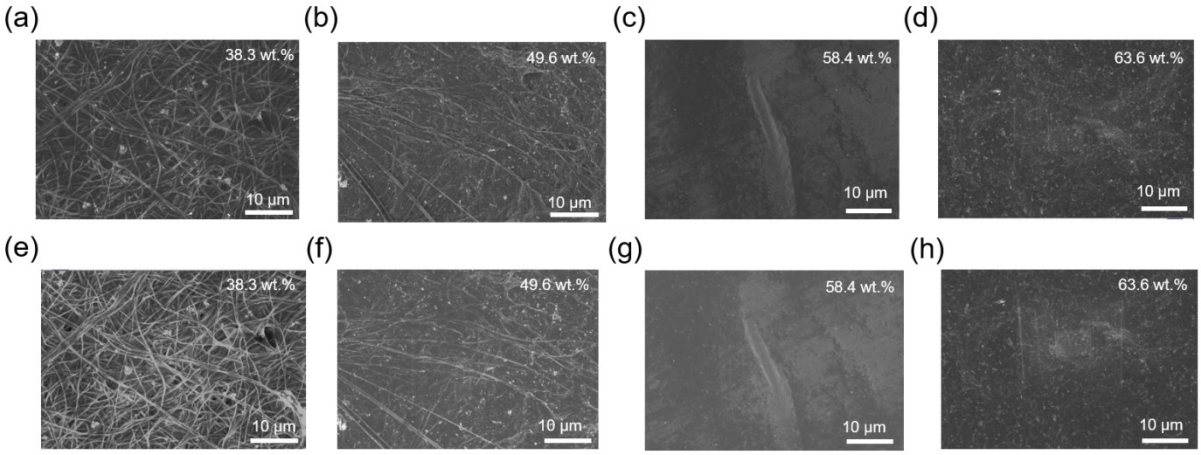

Fig. S19. SEM images of $Ti_3C_2T_x$/MLPAN with different $Ti_3C_2T_x$ content of 38.3 wt.%, 49.6 wt.%, 58.4 wt.% and 63.6 wt.% before (a-d) and after (e-h) 1000-cycles of bending.

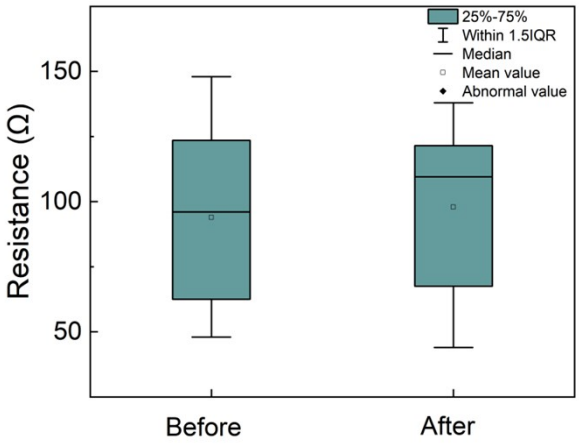

Fig. S20. Resistance of $Ti_3C_2T_x$/MLPAN film before and after soaking in water for 24-hour.

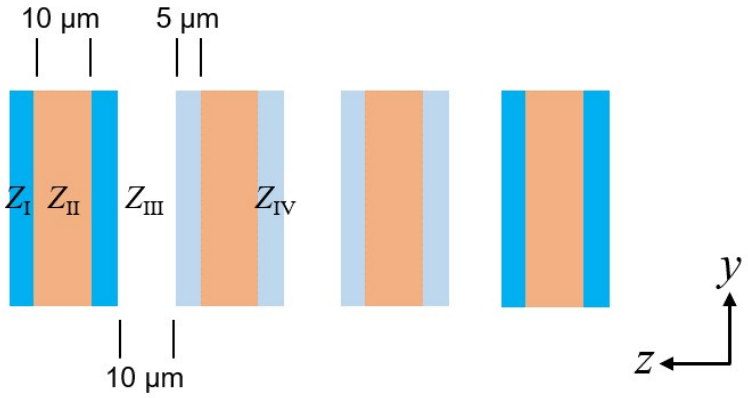

Fig. S21. Structure schematic diagram in CST simulation. X axial and Y axial scales of the structure follow the actual size of 8-12 GHz rectangular wave guide.

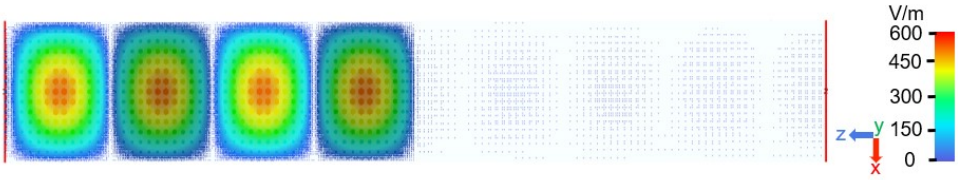

Fig. S22. Top view of electric field simulation result, wherein the incident wave propagates in the negative Z-axis direction.

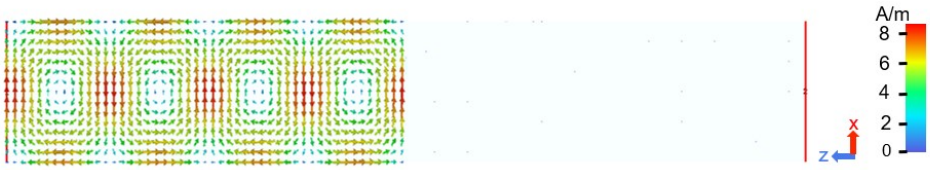

Fig. S23. Top view of magnetic field simulation result, wherein the incident wave propagates in the negative Z-axis direction.

Table S1. SE_{Total} and power coefficient of MLPAN, $Ti_3C_2T_x$, and $Ti_3C_2T_x$/MLPAN with different $Ti_3C_2T_x$ content.

Materials	$Ti_3C_2T_x$ Content [wt.%]	SE_{Total} [dB]	R	A	T
MLPAN	-	5.0×10^{-2}	0.001	0.010	0.988
$Ti_3C_2T_x$/MLPAN	38.3	38.2	0.665	0.334	1.510×10^{-4}
$Ti_3C_2T_x$/MLPAN	49.6	44.4	0.671	0.328	3.500×10^{-5}
$Ti_3C_2T_x$/MLPAN	58.4	51.7	0.679	0.320	6.492×10^{-6}
$Ti_3C_2T_x$/MLPAN	63.6	61.8	0.681	0.318	6.489×10^{-7}
$Ti_3C_2T_x$	100.0	45.5	0.818	0.181	2.798×10^{-5}

Table S2. Details of XPS peak differentiation imitating analysis.

Region	BE (eV)	Assigned to
Ti $2p_{3/2}$ ($2p_{1/2}$)	455 (461.2)	C–Ti–(O/OH)
	455.8 (461.3)	C–Ti^{2+}–(O/OH)
	458.6 (464.2)	TiO_2
	459.3 (465.3)	$TiO_{2-x}F_{2x}$
C1s	281.8	C-Ti
	282.3	Ti-C-O
	284.8	C-C
	286.2	C-O
	288.7	O-C=O
	291.4	π-π*
	286.6	C≡N

References

66 V. Natu, M. Benchakar, C. Canaff, A. Habrioux, S. Célérier and M. W. Barsoum, *Matter*, 2021, **4**, 1224-1251.

67 J. Yan, C. E. Ren, K. Maleski, C. B. Hatter, B. Anasori, P. Urbankowski, A. Sarycheva and Y. Gogotsi, *Advanced Functional Materials*, 2017, **27**, 1701264.

68 C. W. W. S. Bredas, *Synthetic Metals*, 1986, **16**, 147-159.

69 S. A. Schelkunoff, *Bell System Technical Journal*, 1938, **17**, 17-48.

70 R. S. V. P. D. Brush, *IEEE Transactions on Electromagnetic Compatibility* 1988, **30**, 187-201.

71 L. Wang, Z. Ma, Y. Zhang, L. Chen, D. Cao and J. Gu, *SusMat*, 2021, **1**, 413-431.